Elsevier Editorial System(tm) for
Engineering Fracture Mechanics
Manuscript Draft

Manuscript Number:

Title: Hybrid technique to assess the fatigue performance of multiple cracked FSW joints

Article Type: Original Research Paper

Keywords: Friction Stir Welding; Multiple Crack Growth; Residual Stress; DBEM; Contour Method

Corresponding Author: Prof. roberto citarella, PhD

Corresponding Author's Institution: University of Salerno

First Author: roberto citarella, PhD

Order of Authors: roberto citarella, PhD; Pierpaolo Carlone, Prof; Marcello Lepore, Dr.; Raffaele Sepe, Dr.

Abstract: In this paper a numerical-experimental procedure useful to numerically assess the fatigue performance of friction stir welded alluminium joints is presented. The impact of manufacturing residual stresses on crack propagation in the joint, as driven by a remote fatigue load, can be predicted by a sequential procedure that starts with the experimental residual stress measurements by the Contour Method and proceeds through the multiple crack growth simulation by the Dual Boundary Element Method. In the frame of Linear Elastic Fracture Mechanics, the superposition principle is invoked to provide the mathematical foundation supporting the proposed modelling strategy. Simple specimens are fatigue tested and the coming out multiple crack propagation scenario is monitored in order to cross compare experimental and numerical crack growth rates and validate the proposed procedure.

Suggested Reviewers: Francesco Iacoviello Prof.
iacoviello@unicas.it

Ali Fatemi Prof.
University of Toledo Ohio USA
ali.fatemi@utoledo.edu

Cetin Morris Sonsino Prof.
LBF Fraunhofer
c.m.sonsino@lbf.fraunhofer.de

Guido Dhondt Dr.
MTU Aero Engines GmbH
dhondt@t-online.de

Angelo Maligno Dr.
maligno@derby.ac.uk

Cover letter

Dear prof. Meinhard Kuna,

this paper is now resubmitted, after rejection due to excessive overlap with another published paper. The degree of overlap has been substantially reduced and the peculiarities of the paper have been highlighted by adding new paragraphs.

Best Regards,
Prof. Roberto Citarella

Hybrid technique to assess the fatigue performance of multiple cracked FSW joints

R. Citarella[1], P. Carlone[1], M. Lepore[1], R. Sepe[2]

[1]Department of Industrial Engineering, University of Salerno, Fisciano (SA), Italy.

[2]Department of Industrial and Information Engineering, Second University of Naples, Via Roma 29, 81031 Aversa, Italy.

Corresponding author: Roberto Citarella, rcitarella@unisa.it, mobile: +393207406252, office:+39089964111, fax:+39089964037

Abstract

In this paper a numerical-experimental procedure useful to numerically assess the fatigue performance of friction stir welded alluminium joints is presented. The impact of manufacturing residual stresses on crack propagation in the joint, as driven by a remote fatigue load, can be predicted by a sequential procedure that starts with the experimental residual stress measurements by the Contour Method and proceeds through the multiple crack growth simulation by the Dual Boundary Element Method. In the frame of Linear Elastic Fracture Mechanics, the superposition principle is invoked to provide the mathematical foundation supporting the proposed modelling strategy. Simple specimens are fatigue tested and the coming out multiple crack propagation scenario is monitored in order to cross compare experimental and numerical crack growth rates and validate the proposed procedure.

Keywords: Friction Stir Welding, Multiple Crack Growth, Residual Stress, DBEM, Contour Method.

1 Introduction

Design and manufacturing of lightweight assembled structures, characterized by high recycling rate, is currently cutting edge for the transport industries [1]. In this sector, despite the low weight and high specific mechanical properties exhibited by magnesium and titanium alloys, aluminium is still considered as a preferable choice due to cost considerations. Several authors demonstrated effectiveness and efficiency of friction stir welding (FSW) process for joining difficult to weld similar and dissimilar materials pairs [2-4]. FSW is a solid state welding process that allows realising sound joint heating and intimately mixing the adjoining materials by means of a specifically designed non-consumable tool. The combined rotation and translation of the tool locally increase the work piece temperature and then the

softened material is forced to flow around the pin (or probe) resembling an extrusion plastic flow. Simultaneously, it is compressed by the forging action of the shoulder, providing the final material continuity [4]. The solid-state nature of the process implies relevant advantages as process induced residuals stresses, distortions, and microstructure alterations are significantly reduced if compared to what observed in fusion welding processes [4,5]. Nevertheless, taking also into account the lack of hystorical data, the careful assessment of static strength and fatigue properties of welded assemblies appears imperative for a wider structural application of this technique, as discussed in [6-8]. In particular in [7] the effects of crack orientation with respect to the weld line and stress axis were determined, and the influence of heat affected zone (HAZ) microstructure, hardness and residual stress fields was examined; the effects of residual stress reduction using mechanical stress relief were also explored.

Recently, some attempts to numerically assess the fatigue behaviour in friction stir welded structures were commented in literature [9-13]. In particular in [9] an approach based on Boundary Element Method (BEM) was adopted for crack growth simulation. The residual stress relaxation phenomenon was taken into account and a variable calibration for the Paris law was provided depending upon the FSW regimes. Some of the present authors numerically assessed the influence of the residual stress scenario, induced by friction stir welding process, on the crack propagation rate in [11], whereas, in [12], the same procedure was applied to investigate the sensitivity of crack growth rate to processing parameters.

Previous works, however, were limited to the simulation of the relatively simpler case of single crack propagation, whereas in this paper a multiple crack scenario is numerically reproduced by Dual Boundary Element Method (DBEM) [14-18]. DBEM approach turn out to be more efficient than FEM when tackling crack propagation problems under LEFM (Linear Elastic Fracture Mechanics) hypothesis [19-21].

SIFs along the crack front are evaluated by the J-integral technique [22] and a pure mode I criterion is adopted for crack path prediction, consistently with the nearly symmetric applied boundary conditions (no tangential residual stresses are superimposed on crack faces).

The contour method [23] was applied to infer the longitudinal residual stresses acting on the weld cross section. A three dimensional FE linear elastic model has been solved to post-process experimental data, providing the longitudinal stress distribution, as reported in details in [24].

The computed residual stresses field has been superimposed, in a DBEM environment to the stress field due to a remote fatigue traction load and the crack growth is simulated.

A two-parameters crack growth law, previously calibrated for the material under analysis, is used for the crack propagation rate assessment [25, 26].

When the cracks are growing, the stress field profiles around the crack regions slightly change due to plasticity effects whereas, in this work, no allowance was provided during the propagation for such changes. However, following the outcomes of previous work by some of the authors [11, 12, 25, 27, 28], it is possible to state

that such changes are not so relevant for this kind of problems as to invalidate the accuracy of the simulation.

Computational results have been compared with experimental data, provided by constant amplitude crack propagation tests on welded samples.

2 Experimental analysis

2.1 Welding process and specimen set up

The base material used in the present investigation was AA2024-T3 aluminium alloy. Chemical composition, physical and mechanical properties of the selected material are fully available in literature [29]. Rolled strips (200 mm x 60 mm x 4 mm) were butt joined by FSW. The process was realized using Cr-Mo steel tools, characterized by a flat shoulder and a conical unthreaded probe. Fig. 1 shows the welding setup. Probe dimensions, namely major diameter, length and cone angle, were defined as 6.2 mm, 3.8 mm, and 30°, respectively. Shoulder diameter was defined as 20 mm. The welding process was performed imposing rotational and welding speeds equal to 1400 rpm and 70 mm/min respectively and tilting the tool axis 2° to enhance the shoulder forging action.

In order to speed up and localise the crack initiation, an initial edge notch with a length equal to 2 mm was cut by Wire Electro-Discharge Machining (WEDM) on the retreating side of the weld, at the middle length of the specimen (Fig. 2). Two crack gages were applied on both sides of the notch in order to automatically monitor the advancing crack. The crack growth was monitored using crack propagation patterns TK-09-CPA01-005/DP of MM Vishay, applied on both sides (CG1 and CG2) of the specimen in correspondence of the lateral notch. The fatigue test set up is shown in Fig. 2.

Fig. 1. Welding setup.

Fig. 2. Experimental set-up with highlight of notch and crack gauge.

2.2 Fatigue test

Fatigue tests were performed using a universal testing machine INSTRON 8502 with a load cell range equal to 250 kN. A fatigue load Pmax = 24 kN, corresponding to a remote stress □ = 100 MPa, was applied with a frequency equal to 10 Hz and a load ratio R = 0.1.

The tested specimen exhibited a crack initiation in correspondence of the notch (as expected) but also in a position different than the notch area, in correspondence of the weld crown. This was attributed to the excessive heating of the tool, promoting the adhesion of the plasticized material on the tool shoulder resulting in a rough aspect of the crown. Such condition produced a multiple crack scenario realised by a central crack and a lateral crack (Figs. 3a-c).

The analysed specimen exhibited prevailing crack propagation from the semi elliptical defect in the middle of weld crown rather than from the lateral notch. The experimental fatigue life was equal to 355380 cycles, with a fatigue crack advance monitored just from the lateral notch because no crack gauges were applied in correspondence of the central crack.
A post-mortem metallographic analysis of the specimen fracture surface provided the initial cracks to be introduced in the numerical model. The separation between the fatigue crack propagation area (black arrows) and the area of static ductile failure (outside green dot lines), and the separation between the initial defect (red line) and crack propagation area are clearly visible in Figs. 3a-c. The fatigue crack growth, as expected, proceeded under nearly pure mode I, whereas just the ductile static failure (after reaching an instability condition) exhibited an inclined fracture surface (Fig. 3d). In particular, the subcritical fatigue crack propagation involves only about one third of the specimen width, the central part in correspondence of the welded zone: as the crack propagates through the thickness it also cuts through the weld zone along the width direction, in such a way that as soon as the crack becomes through the thickness SIFs along the crack front get so high to produce crack growth instability followed by a slant ductile rupture. Consequently the only phase that can be simulated is the part through crack growth that develops with nearly no appreciable kinking (the slight kinking visible from Fig. 3b can be attributed to a slant plastic rupture happening when the crack is on the verge to break through the thickness).

Fig. 3. Specimen with cracked initial scenario based on a secondary through crack from the notch (a-b), and a main semi elliptical crack (red line in c) initiated from the centre of weld crown (b-c). In (d) highlight of in plane crack propagation with nearly no kinking, but for the final ductile break through rupture.

In details, crack gauges evidenced:

1) the crack initiation from the notch after 339000 fatigue cycles, with an initial crack length equal to 2.25 mm (2 mm notch + 0.25 mm precracking);
2) a relatively slow initial propagation lasting 14000 cycles with a crack advance equal to 0.25 mm;
3) a sudden acceleration of the aforementioned lateral crack.

The explanation of such sharp increment in the lateral crack growth rates can be reconducted to the initiation and rapid propagation of the central through crack, with consequent multiple site damage (MSD) scenario; this hypothesis will be validated by the simulations discussed in the following.
Even if there is a first crack wire adjacent to the notch tip, the related rupture was not considered indicative of a crack formation, whereas the crack is considered initiated only after a pre-cracking phase ending when the rupture of the second crack wire indicated that a minimal precrack phase was accomplished. The crack wire pitch is equal to 0.25 mm so that the initial modelled crack is equal to 2.25 mm (corresponding to the second crack wire breakage).

3 Numerical analysis

3.1 Theoretical aspects of crack growth simulation by DBEM

In the following a description of numerical implementation of the DBEM for crack-growth problems examined through the linear elastic fracture mechanics is provided [30-31]. The dual boundary integral equations are presented and the crack modelling strategy is defined.

The dual boundary element method allows to analyse general crack problems to be performed through a single-region boundary element formulation. The dual equations, on which the DBEM is based, are the displacement and the traction boundary integral equations. Throughout this work, the Cartesian tensor notation and Einstein's summation convention are used. In the absence of body forces, the boundary integral representation of the displacement components u_i at a source point x' on the boundary is given by

$$c_{ij}(x')\cdot u_j(x')+\int_\Gamma T_{ij}(x',x)\cdot u_j(x)\cdot d\Gamma(x)=\int_\Gamma U_{ij}(x',x)\cdot t_j(x)\cdot d\Gamma(x) \qquad (1)$$

where $c_{ij}(x')$ is a coefficient depending on the geometry in the source point, and the integral on the left side is calculated in the Cauchy principal-value sense. $U_{ij}(x',x)$ and $T_{ij}(x',x)$ are the Kelvin fundamental solutions. The traction components t_j are given by

$$\frac{1}{2}t_j(x')+n_j(x')+\int_\Gamma S_{ijk}(x',x)\cdot u_k(x)\cdot d\Gamma(x)=n_i(x')\int_\Gamma D_{ijk}(x',x)\cdot t_k(x)\cdot d\Gamma(x) \qquad (2)$$

where n_i denotes the i-th component of the unit outward normal to the boundary at the source point. The integral on the left side is to be considered in the Hadamard sense whilst that on the right side in the Cauchy principal-value sense. Equations (1) and (2) constitute the basis of the DBEM.

The necessary conditions for the existence of the principal-value integrals obtained in the derivation of the dual boundary integral equations impose restrictions on the discretisation. Consider that both geometry and boundary field variables are described by a piece-wise continuously differentiable approximation and the collocation process is always performed with the source point at the boundary element nodes.

Under these considerations, the continuity requirements of the Cauchy principal-value integral in the displacement equation can be satisfied by any Lagrangian continuous or discontinuous boundary element. However, in the traction equation the continuity requirements of the Hadamard principal-value integral are satisfied only by discontinuous elements, since all the nodes are internal points of the element where a continuously differentiable approximation is defined. Moreover, the requirement of the smoothness of the geometry at a collocation point in the traction equation is implicitly satisfied by the discontinuous element. Furthermore, discontinuous traction fields can be modelled by discontinuous elements, since the tractions must satisfy Hölder continuity only at the nodes. It is important to realise that, if the element approximation does not satisfy these necessary continuity

requirements, then the finite-part integrals do not exist. For the sake of efficiency and to keep the simplicity of the standard boundary elements, the present formulation uses discontinuous quadratic elements for crack modelling.
The general modelling strategy can be summarised as follows:

- The traction (Eq. 2) is applied for collocation on one of the crack boundaries;
- The displacement (Eq. 1) is applied for collocation on the opposite crack boundary and remaining boundaries;
- The crack boundaries are discretised with discontinuous quadratic elements;
- Continuous quadratic boundary elements are used along the remaining boundaries of the problem domain, except at the intersection between a crack and an edge, where discontinuous or semi-discontinuous elements are required, in order to avoid nodes at the intersection.

This simple strategy is robust and allows the DBEM to effectively model general edge or embedded crack problems. Crack tips, crack-edge corners and crack kinks do not require a special treatment, since they are not located at nodal points where the collocation is carried out.

3.2 Crack growth law

According to the Vasudevan approach [26], fatigue crack growth is driven by two driving forces, K_{max} and ΔK, with corresponding fatigue thresholds, $K^*_{max,th}$ and ΔK^*_{th}: both the driving forces must be simultaneously larger than the relative thresholds for fatigue crack growth to occur.
The crack growth law (Eq. 3) is assumed as follows [25, 26]:

$$da/dN = A\cdot(\Delta K - \Delta K_{th})^n\cdot(K_{max} - K_{max,th})^m \quad (3)$$

and is calibrated by best fitting the material parameters A, n, m based on literature data [11,12]. Used parameters are listed in Table 1 and are valid for positive R-ratio.

Table 1. Crack propagation law parameters

ΔK^*_{th} [N/m$^{3/2}$]	$K^*_{max,th}$ [N/m$^{3/2}$]	A [m$^{1.5\cdot(n+m)+1}$/N^{n+m}]	n	m
1834121	3352014	6.745E-23	1.65	0.56

In Eq. (3) SIFs are defined as the sum of the nominal SIF, corresponding to the remote load, and of the SIF corresponding to residual stresses acting on crack faces and induced by the friction stir welding process.
The pre-existing residual stress scenario was superimposed to the stress state caused by the remote traction load following the Bueckner approach [32]. In particular, the residual stress effect was modelled as a distribution of tractions applied on the crack faces. Such tractions were obtained measuring the longitudinal residual stresses (direction parallel to the weld line) in welded samples, by means of the contour method. The adopted procedure is fully detailed elsewhere [24]. The stress map,

inferred in the herein discussed case, is depicted in Fig. 4 in the interest of completeness. Young modulus and Poisson ratio of the adopted material are equal to 73.3 GPa and 0.33, respectively.

Fig. 4. Longitudinal residual stress (σ_{zz}) distribution. The crack notch was realised at the left edge at x = -30 mm (retreating side of the weld) and the central semi elliptical crack initiated in the upper side at x = 0 mm and y = 4 mm.

3.3 Procedure description

3.3.1 Theoretical background

When the plastic deformations are sufficiently small the hyphotesis of LEFM holds true and consequently the superposition principle stands. Under such conditions it is possible to state that the effect of residual stresses on a crack in a body can be assessed by modelling the same cracked body without residual stresses in any part of the domain and with just a distributed load applied on the crack faces; such load is that corresponding to the aforementioned residual stresses in the uncracked body, along the virtual line/surface depicted by the advancing crack (Fig. 5). In the framework of aforementioned hyphotesis there is the allowance for residual stress redistribution as a consequence of crack propagation. As a matter of fact, looking at the *C'* problem (which is the problem to be solved) depicted in Fig. 5, it is possible to see that the residual stress state is not the original one (evaluated on the uncracked body) but is modified by the superposition of $\sigma'[-t(\sigma_0)]$.

Fig. 5. Superposition principle for SIFs assessment.

3.3.2 Overall procedure

The residual stresses in the main crack section, stored in the ANSYS .rst result file, were imported in the commercial suite BEASY [33] for the DBEM crack propagation analysis, driven by the remote fatigue load (= 100 MPa) and by the superimposed (on the crack faces) residual stress scenario. A flowchart explaining the overall procedure is shown in Fig. 6.

Fig. 6. Overall procedure flowchart.

The DBEM model was clamped on one end and loaded on the opposite end and on the crack faces (Fig. 7).
The hypothesis to be verified by the simulations is that initially only the lateral crack is present, whereas the timing of central crack initiation and rapid propagation is coincident with the sudden acceleration of lateral crack growth highlighted by the crack gauges (at nearly 13500 cycles). Resorting to an hybrid approach, where the simulations complement the incomplete information from experiments (no crack gauges were available to monitor the unexpected central crack initiation and

propagation) is a powerful tool to get exhaustive information on the fracture phenomenon.
The contour method procedure makes available the residual stress profile, for automatic insertion in the DBEM environment, only with reference to the main crack section, consequently, the lateral crack was loaded with an approximate distribution of constant compressive residual stresses as shown in Fig. 7 (in reality such stresses are spatially varying as visible from Fig. 4). The magnitude of such constant value (43 MPa) is obtained by calibration, imposing that the numerical lateral crack growth rates be equal to the experimental crack growth rates in the range from 2.25 mm to 2.50 mm crack length. At this stage the central crack has not yet reached appreciable sizes so that it is not modelled at all (Fig. 7).

Fig. 7. DBEM single crack model with highlight of Von Mises stresses [Pa]: the crack length is equal to 2.5 mm and the deformation scale equal to 100.

After nearly 13500 fatigue cycles of lateral crack propagation in a single crack scenario, the second crack was postulated to initiate from a defect at the middle of the weld crown (as previously mentioned there were no crack gauges applied in that area) as shown in Fig. 3c. This is very likely to happen at this point because, otherwise, the lateral crack alone would continue its numerical propagation with non-realistic crack growth rates, as shown in Fig. 8 (here only the crack advance recorded by the crack gauge CG1 is displayed, because the related data were very similar to those recorded by CG2). On the contrary, the thumbnail crack initiation and propagation, produced a clear acceleration on the lateral crack in the numerical simulation, consistently with experimental outcomes (Fig. 8).

Fig. 8. Lateral crack advance as monitored by CG1 crack gauge and as calculated by DBEM in case of no added central crack (one crack) or with added central crack (two crack scenario) after nearly 13500 cycles.

The initial numerical multiple crack configuration (Fig. 9) is based on a semielliptical crack (N. 1) and a through crack (N. 2), respectively initiated from a weld crown defect and from the lateral notch (Figs. 3a-c). The semielliptical crack has major and minor semi-axes equal to 5.5 mm and 1.7 mm respectively, as provided by a fractographic post mortem analysis of the specimen failure section (red line in Fig. 3c).
The average crack advance along the crack front and at each step is equal to 0.4 mm. The mesh density during the through the thickness crack propagation varies from 1480 to 3220 elements with reference to the initial and final configuration respectively, with a mixed mesh based on reduced quadratic (the node at the element center is missing) and triangular quadratic elements.

Fig. 9. DBEM initial (up) and final (down) multiple crack configuration with highlight of Von Mises stresses [Pa] and deformation scale equal to 50.

In Fig. 10 the through the thickness crack propagation is showed with highlight of the growing crack and of the related residual stresses, applied as normal tractions on the crack faces. The thumbnail crack, initiating from the middle of weld crown, grew mainly within the nugget zone and thermo-mechanical affected zone but also in the heat affected zone for the final part, whereas the lateral through crack grew within the parent material zone.

Fig. 10. Contour plot of normal tractions on the crack faces for each crack advance (the scale for the central crack contour is different than that for the lateral crack), with highlight of j-path and sizing points (A, B, C) along the crack front.

The central crack propagation turned out to be responsible for specimen failure, because SIFs calculated for the lateral crack (Fig. 11) were not sufficiently higher than threshold ($K_{max,th}$ = 3352014 Pa·m$^{0.5}$) to produce appreciable advances (Fig. 12). After four crack growth steps (Fig. 10) the simulation reproduced the experimental condition of crack instability (there is not plastic collapse yet, as visible from Fig. 8 and considering that the yielding stress is equal to σ_y = 395 MPa), with a central crack that cut the whole welding in the thickness direction. The semielliptical crack becomes through the thickness after nearly 3600 cycles (Fig. 12) with a nearly symmetric advance on both the advancing and retreating sides (the residual stress slight asymmetry has a negligible impact on the overall crack behaviour).

Fig. 11. K_I (Pa·m$^{0.5}$) along the crack front for each step of crack propagation: curivilinear abscissa from 0 to 1 for crack N.1 (a) and from 1 to 2 for crack N. 2 (b). ("inc" = "step" indicates the varying increment during the propagation).

Fig. 12. Crack sizes (mm) for the semielliptical crack (measured at the size points A, B, C) and for the lateral through crack ("size A" is that measured at the crack gauge CG1 location), against number of cycles.

It is interesting to observe that the final numerical central crack configuration is consistent with the experimental crack scenario at instability (Fig. 13). The final numerical central crack front keeps an elliptical shape (as driven by the residual stresses across the thickness) with a length of the major axis equal to nearly 14 mm (Figs. 10, 12).
The specimen failure is forecasted after a crack propagation phase given by:
13500 (single crack scenario) + 3600 (double crack scenario) =17100 cycles so that crack initiation time for the central semielliptical crack can be estimated at 355000-17100=337900 cycles.
The experimental countercheck for such an estimate comes from the combined use of data from the crack gauges placed at the lateral notch and from the simulations. It is interesting to observe that by a combined use of simulations and available crack gauge recording it is possible to assess the initiation time of the semi elliptical crack in the middle of weld, even if for the latter no crack gauge outcomes are available.

Fig. 13. Cross comparison between the last numerical central crack scenario and the specimen failure section, displaced with the initiation sides facing each other in order to facilitate the comparison. The red dot line highlights the initial part of the ductile rupture when the fracture toughness is reached.

5. Conclusions

The crack propagation scenario emerging from the experimental tests, qualitatively confirmed the residual stress distribution evaluated by the contour method.
From a *post mortem* metallographic analysis the initial defect was clearly pointed out, allowing the definition of a realistic initial crack scenario for the numerical simulation: in particular the correspondance between sizes and fatigue cycles of the initial modelled cracks was in part postulated and a posteriori verified thanks to the numerical simulation outcomes.

The comparison among numerical and experimental results was satisfactory assessed, based on the following observation:

1. the sudden acceleration of the lateral crack was succesfully explained by the initiation and rapid propagation of the central crack, that, introduced in the model with the proper timing, provided a multiple crack scenario evolving consistently with the experimental outcomes;
2. the final numerical crack scenario was comparable with the fatigue area (crack propagation area before instability specimen failure) highlighted by specimen post-mortem fractography;
3. the expected pure mode I crack propagation was confirmed by the experimental fracture surface.

Further development will address the drawbacks of a unique crack growth law calibration for all the different simultaneously propagating cracks, whereas, when such cracks are located in different process zones (nugget zone, thermo-mechanical affected zone, heat affected zone and base material) a variable calibration for the Paris law would be necessary to improve accuracy.

References

[1] Schmidt W.P., Dahlqvist E., Finkbeiner M., Krinke S., Lazzari S., Oschmann D., Pichon S., Thiel C., Life cycle assessment of lightweight and end-of-life scenarios for generic compact class passenger vehicles. The International Journal of Life Cycle Assessment 2004, 9(6): 405-416.
[2] Thomas W.M., Nicholas E.D., Friction stir welding for the transportation industries. Materials and Design 1997; 18(4–6): 269–273.
[3] Carlone P., Astarita A., Palazzo G.S., Paradiso V., Squillace A., Microstructural aspects in Al–Cu dissimilar joining by FSW. International Journal of Advanced Manufacturing Technology 2015; 79 (5-8): 1109-1116.
[4] Mishra R.S., Ma Z.Y., Friction stir welding and processing. Materials Science and Engineering R 2005; 50: 1–78.

[5] Carlone P., Palazzo G.S., Characterization of TIG and FSW weldings in cast ZE41A magnesium alloy. Journal of Materials Processing Technology 2015; 215: 87-94.
[6] Paulo R.M.F., Carlone P., Valente R.A.F., Teixeira-Dias F., Palazzo G.S., Influence of friction stir welding residual stresses on the compressive strength of aluminium alloy plates. Thin-Walled Structures 2014; 74: 184-190.
[7] Bussu G., Irving P.E., The role of residual stress and heat affected zone properties on fatigue crack propagation in friction stir welded 2024-T351 aluminium joints. International Journal of Fatigue 2003; 25: 77–88.
[8] Moreira P.M.G.P., de Oliveira F.M.F., de Castro P.M.S.T., Fatigue behaviour of notched specimens of friction stir welded aluminium alloy 6063-T6. Journal of Materials Processing Technology 2008; 207(1–3): 283–292.
[9] Živojinović D., Đurđević A., Grbović A., Sedmak A., Rakin M., Numerical Modelling of Crack Propagation in Friction Stir Welded Joint Made of Aluminium Alloy. Procedia Materials Science 2014; 3: 1330–1335.
[10] Zadeh M., Ali A., Golestaneh A.F., Sahari B.B., Three dimensional simulation of fatigue crack crowth in friction stir welded joints of 2024-t351 Al alloy, Journal of Scientific & Industrial Research 2009; 68: 775-82.
[11] Carlone P., Citarella R., Lepore M., Palazzo G.S., A FEM-DBEM investigation of the influence of process parameters on crack growth in aluminum friction stir welded butt joints. International Journal of Material Forming 2014, DOI: 10.1007/s12289-014-1186-7.
[12] Citarella R., Carlone P., Lepore M., Palazzo G.S., Numerical–experimental crack growth analysis in AA2024-T3 FSWed butt joints, Advances in Engineering Software 2015; 80: 47–57.
[13] Sepe R., Armentani E., di Lascio P., Citarella R., Crack growth behaviour of welded stiffened panel, Procedia Engineering 2015; 109: 473-483.
[14] Calì C., Citarella R., Perrella M., Three-dimensional crack growth: numerical evaluations and experimental tests, European Structural Integrity Society 31 (2003) 3-504, Biaxial/Multiaxial Fatigue and Fracture, Edited by Andrea Carpinteri, Manuel de Freitas and Andrea Spagnoli.
[15] Citarella R., Perrella M., Multiple surface crack propagation: numerical simulations and experimental tests, Fatigue and Fracture of Engineering Material and Structures 28 (2005), 135-148.
[16] Armentani E., Citarella R., Sepe R., FML Full scale aeronautic panel under multiaxial fatigue: experimental test and DBEM simulation, Engineering Fracture Mechanics, (2011) Vol. 78 Is. 8, pp. 1717-1728.
[17] Leonel E.D., Venturini W.S., Multiple random crack propagation using a boundary element formulation, Engineering Fracture Mechanics, v. 78, p. 1077-1090, 2011.
[18] Oliveira H.L., Leonel, E.D., Dual BEM Formulation Applied to Analysis of Multiple Crack Propagation. Key Engineering Materials, v. 560, p. 99-106, 2013.
[19] Citarella R., Cricrì G., Lepore M., Perrella M., DBEM and FEM Analysis of an Extrusion Press Fatigue Failure. In: A. Öchsner, L.F.M. da Silva, H. Altenbach (eds.), Materials with Complex Behaviour–Advanced Structured Materials, 2010, Vol. 3, Part 2, 181-191. Springer-Verlag, Berlin, Germany, 2010.

[20] Citarella R., Buchholz F.-G., Comparison of crack growth simulation by DBEM and FEM for SEN-specimens undergoing torsion or bending loading, Engineering Fracture Mechanics 75 (2008) 489–509.
[21] Citarella R., Cricrì G., Comparison of DBEM and FEM Crack Path Predictions in a notched Shaft under Torsion, Eng. Fracture Mechanics 77 (2010) 1730-1749.
[22] Rigby R.H., Aliabadi M.H., Decomposition of the mixed-mode J-integral – revisited. Int J Solids Struct 1998; 35(17): 2073–99.
[23] Prime M.B., Cross-sectional mapping of residual stresses by measuring the surface contour after a cut, J. Eng. Mater.-T 2001; 123: 162-168.
[24] Carlone P., Palazzo G.S., Longitudinal Residual Stress Analysis in AA2024-T3 Friction Stir Welding. The Open Mechanical Engineering Journal 2013; 7:18-26.
[25] Citarella R., Cricrì G., A two-parameter model for crack growth simulation by combined FEM-DBEM approach. Adv Eng. Softw 2009; 40: 363-377.
[26] Sadananda K., Vasudevan A.K., Short crack growth and internal stresses. Int. J. Fatigue 1997; 19: 99-108.
[27] R. Citarella, P. Carlone, R. Sepe, M. Lepore, DBEM crack propagation in friction stir welded aluminum joints, Advances in Engineering Software (2016), doi:10.1016/j.advengsoft.2015.12.002.
[28] R. Citarella, G. Cricrì, M. Lepore, M. Perrella, Assessment of Crack Growth from a Cold Worked Hole by Coupled FEM-DBEM Approach, Key Engineering Materials Vols. 577-578 (2014) pp 669-672 © (2014) Trans Tech Publications, Switzerland.
[29] ASM Specialty Handbook: Aluminum and Aluminum Alloys.
[30] Mi Y., Aliabadi M.H., Three-dimensional crack growth simulation using BEM. Comput Struct 1994, 52(5): 871-878.
[31] Cisilino A.P., Aliabadi M.H., Dual boundary element assessment of three-dimensional fatigue crack growth. Eng An Bound El, 2004, 28(9): 1157-1173).
[32] Bueckner H.F., The propagation of cracks and the energy of elastic deformations. Transaction of the ASME 1958; 80: 1225-1230.
[33] BEASY V10r14, Documentation, C.M. BEASY Ltd; 2011.

Highlights

The FEM-DBEM approach proved to be able to predict multiple crack growth in presence of residual stresses.
The crack starts from the weld line the process induced opening stresses play an accelerating effect on the crack propagation.
The numerical results are in good according with experimental measurement.
The presence of residual stresses influences the crack propagation.

***Nomenclature**

DBEM= Dual Boundary Element Method

FSW=Friction Stir welding

TMAZ= thermo-mechanical affected zone

HAZ=heat affected zone

FEM= Finite element method

MSD=Multi site damage

Table

Table 1. Crack propagation law parameters

ΔK^*_{th} [N/m$^{3/2}$]	$K^*_{max,th}$ [N/m$^{3/2}$]	A [m$^{1.5\cdot(n+m)+1}$/N^{n+m}]	n	m
1834121	3352014	6.745E-23	1.65	0.56

Figure 1

Click here to download high resolution image

Figure 2

Click here to download high resolution image

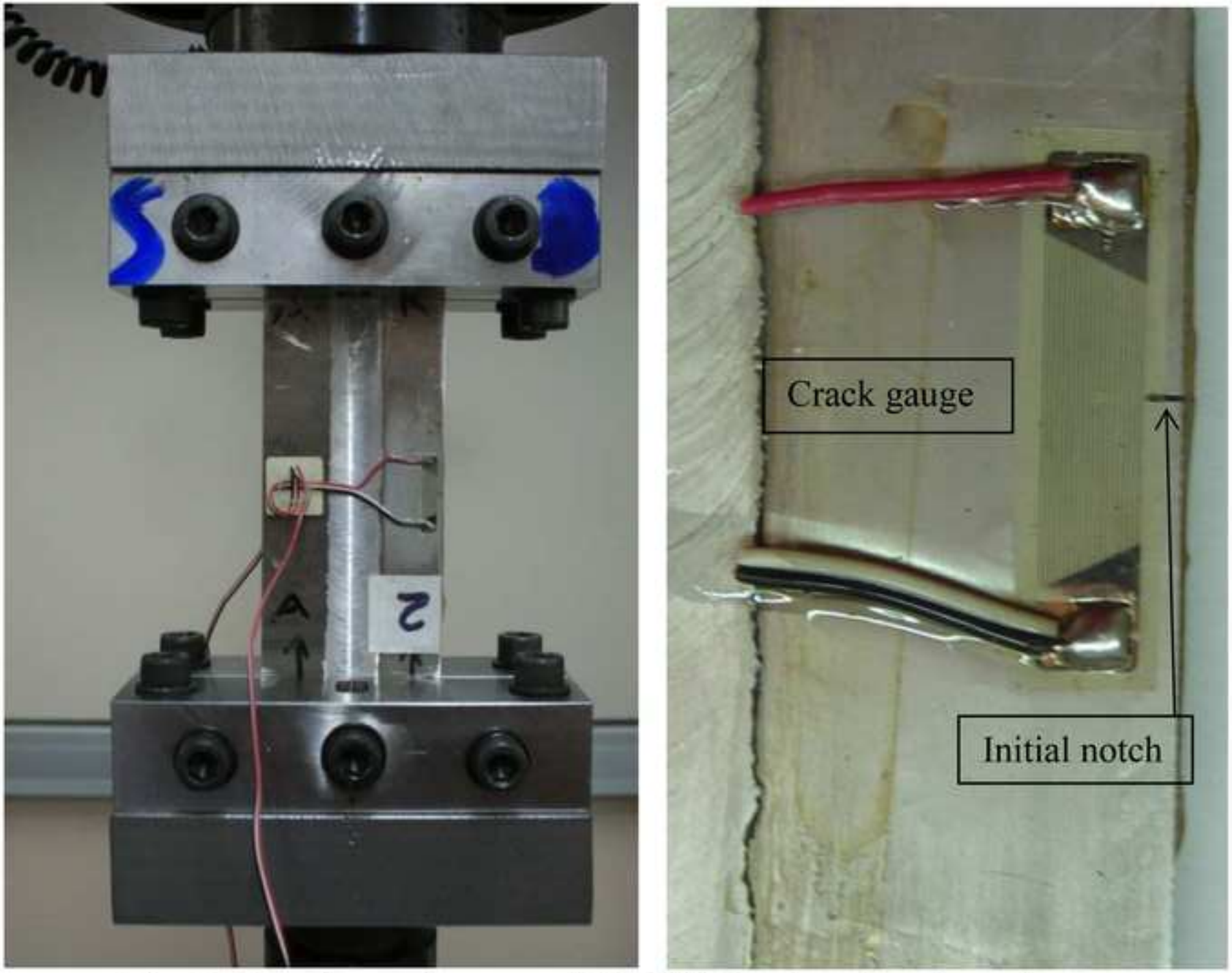

Figure 3

Click here to download high resolution image

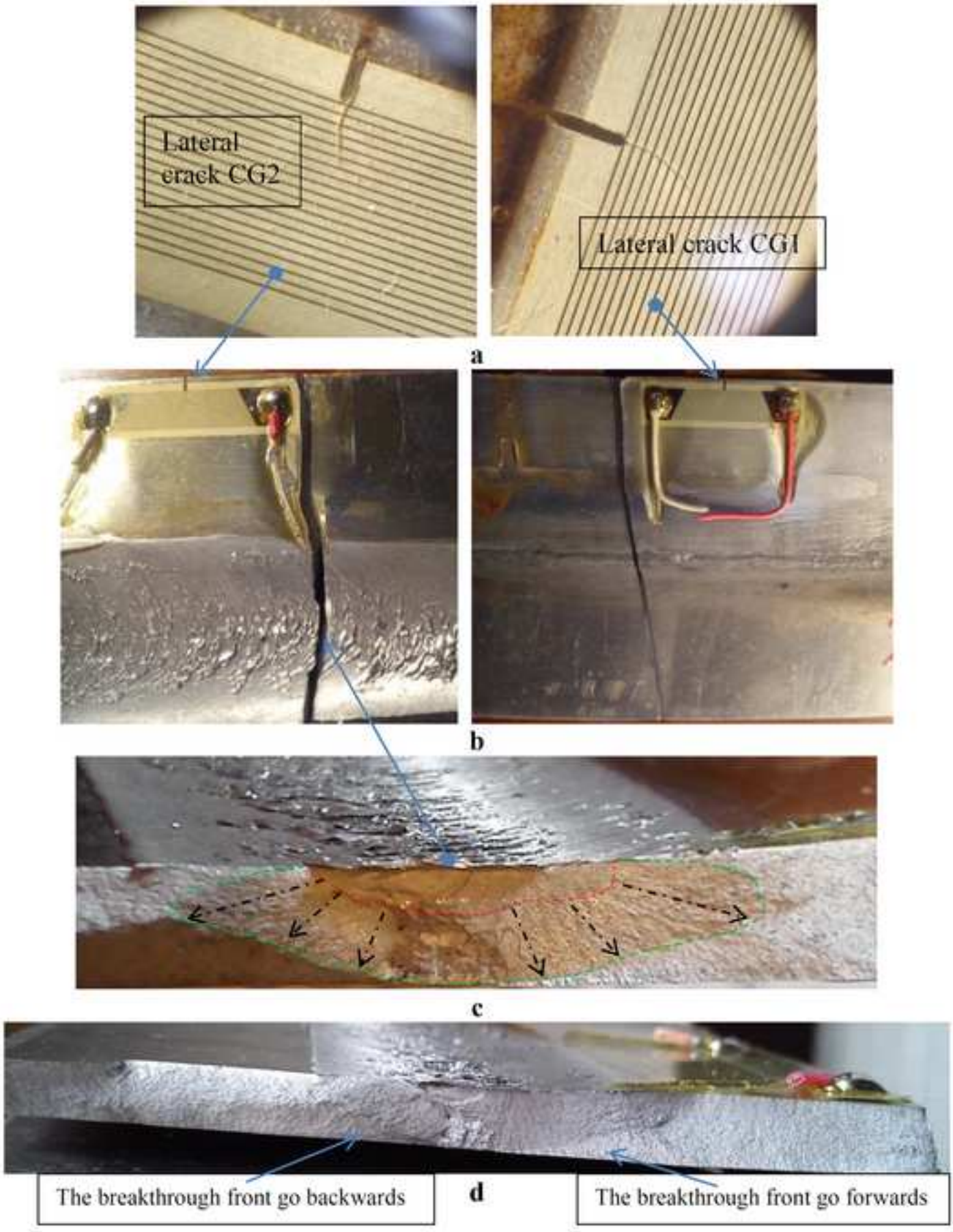

Figure 4

Click here to download high resolution image

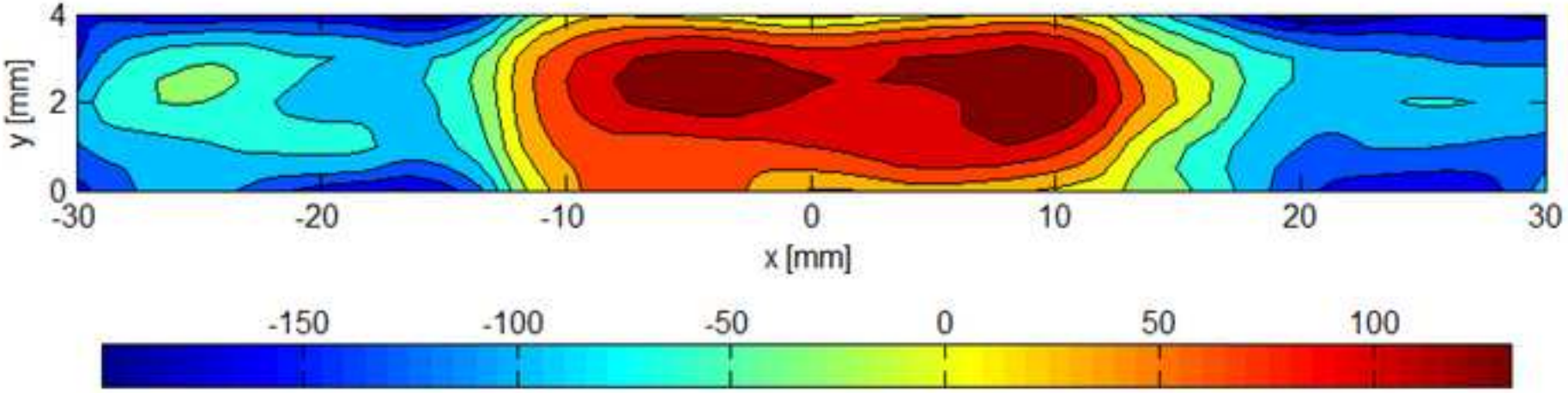

Figure 5

Click here to download high resolution image

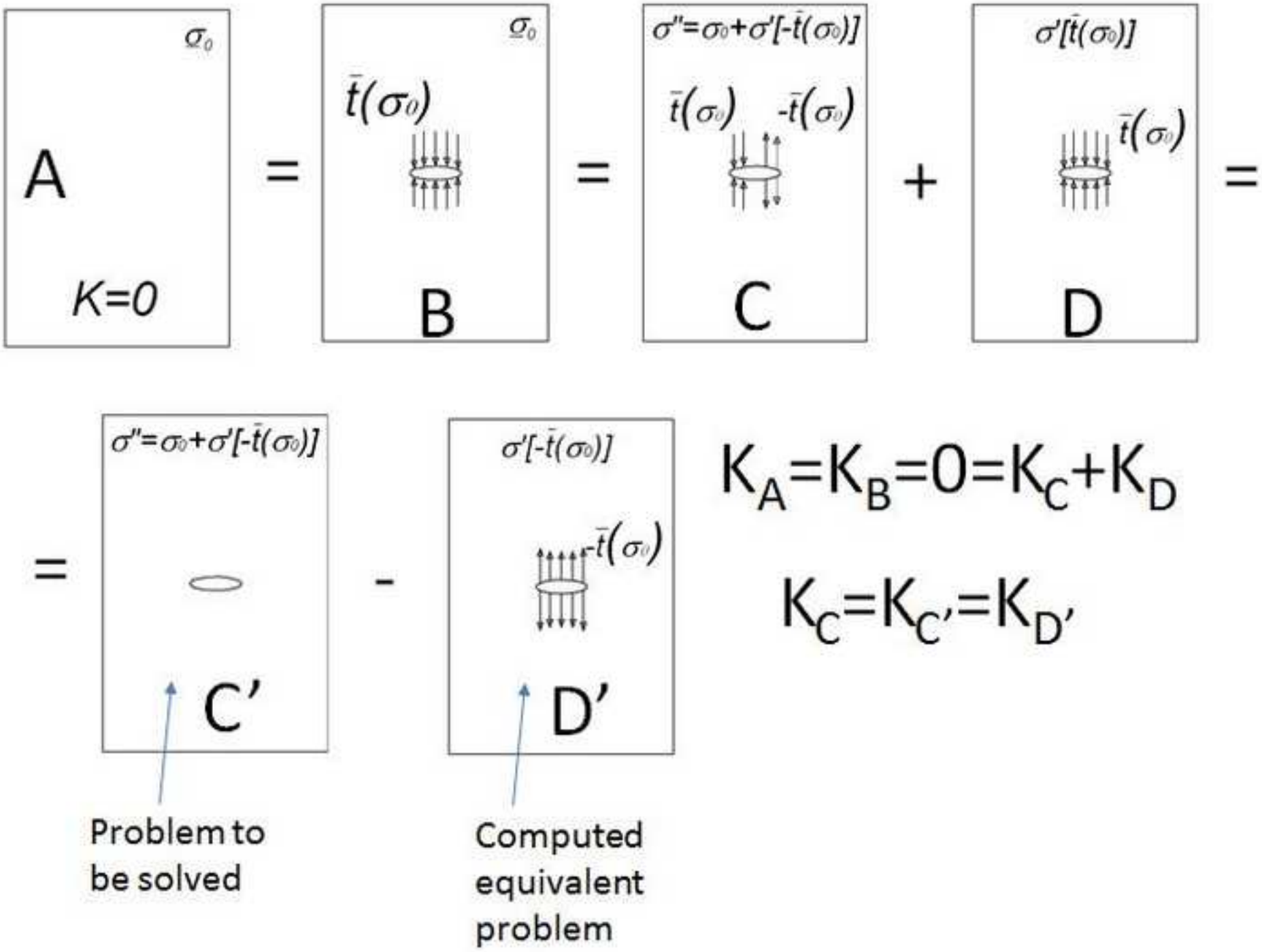

Figure 6

Click here to download high resolution image

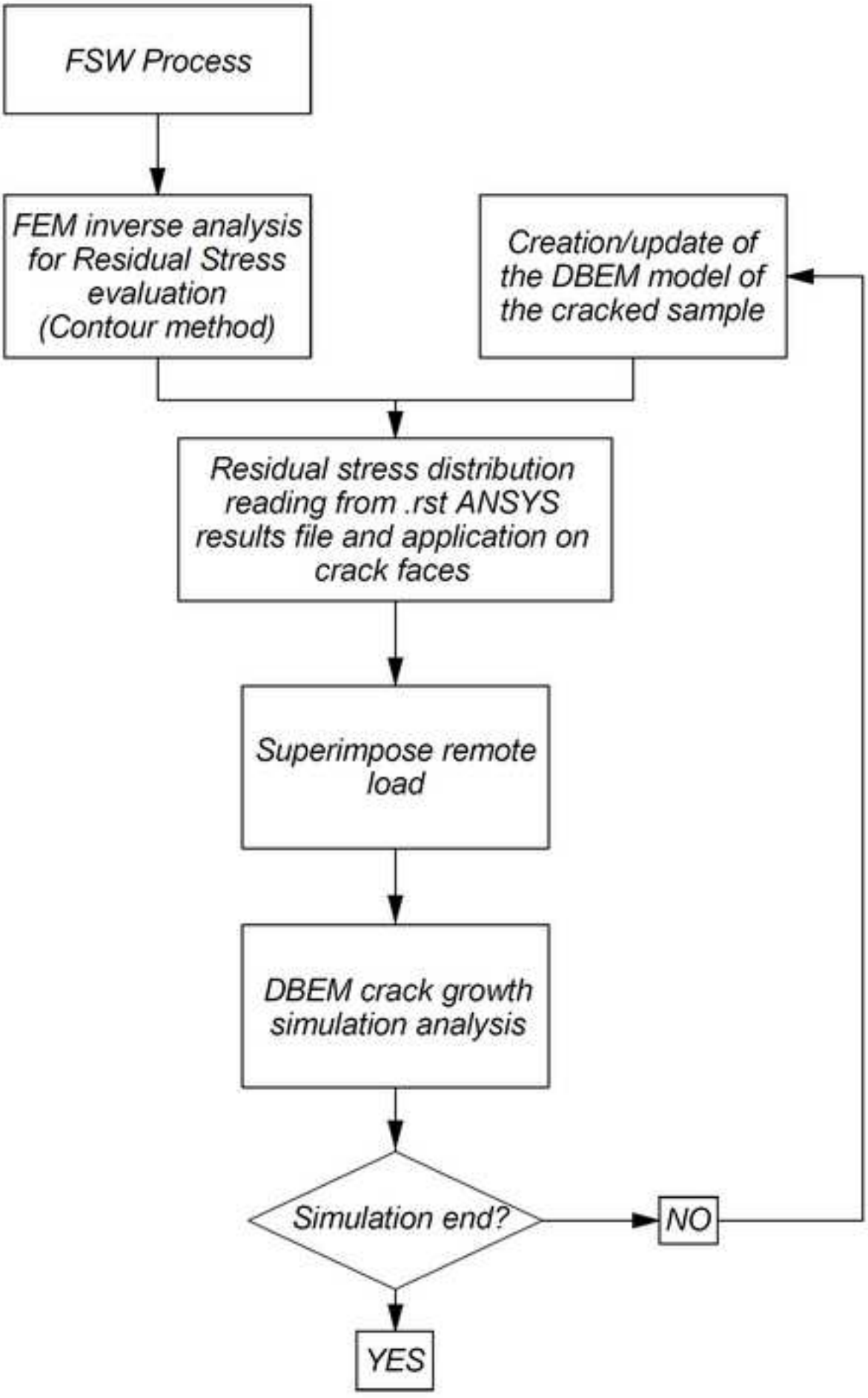

Figure 7

Click here to download high resolution image

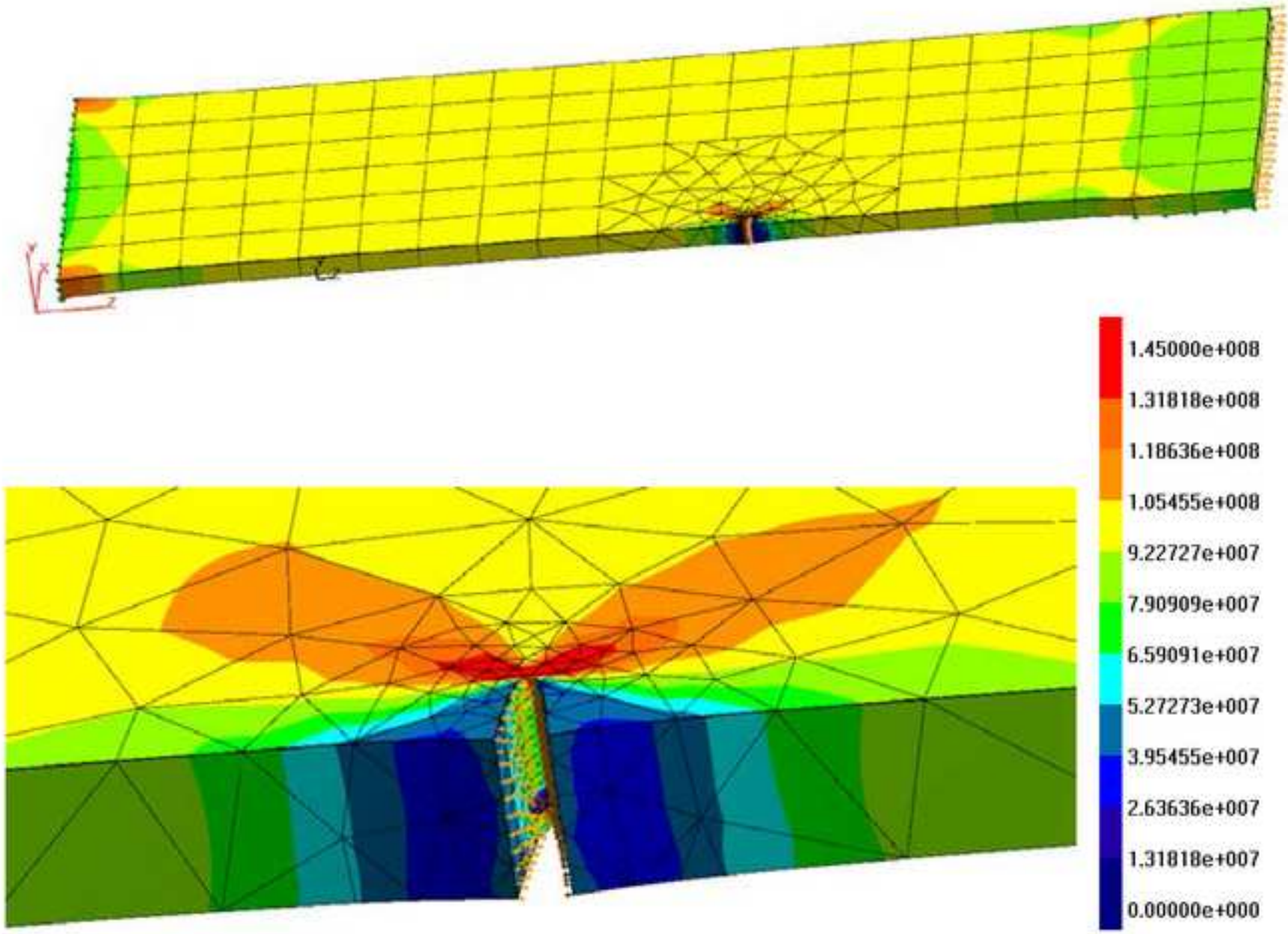

Figure 8

Click here to download high resolution image

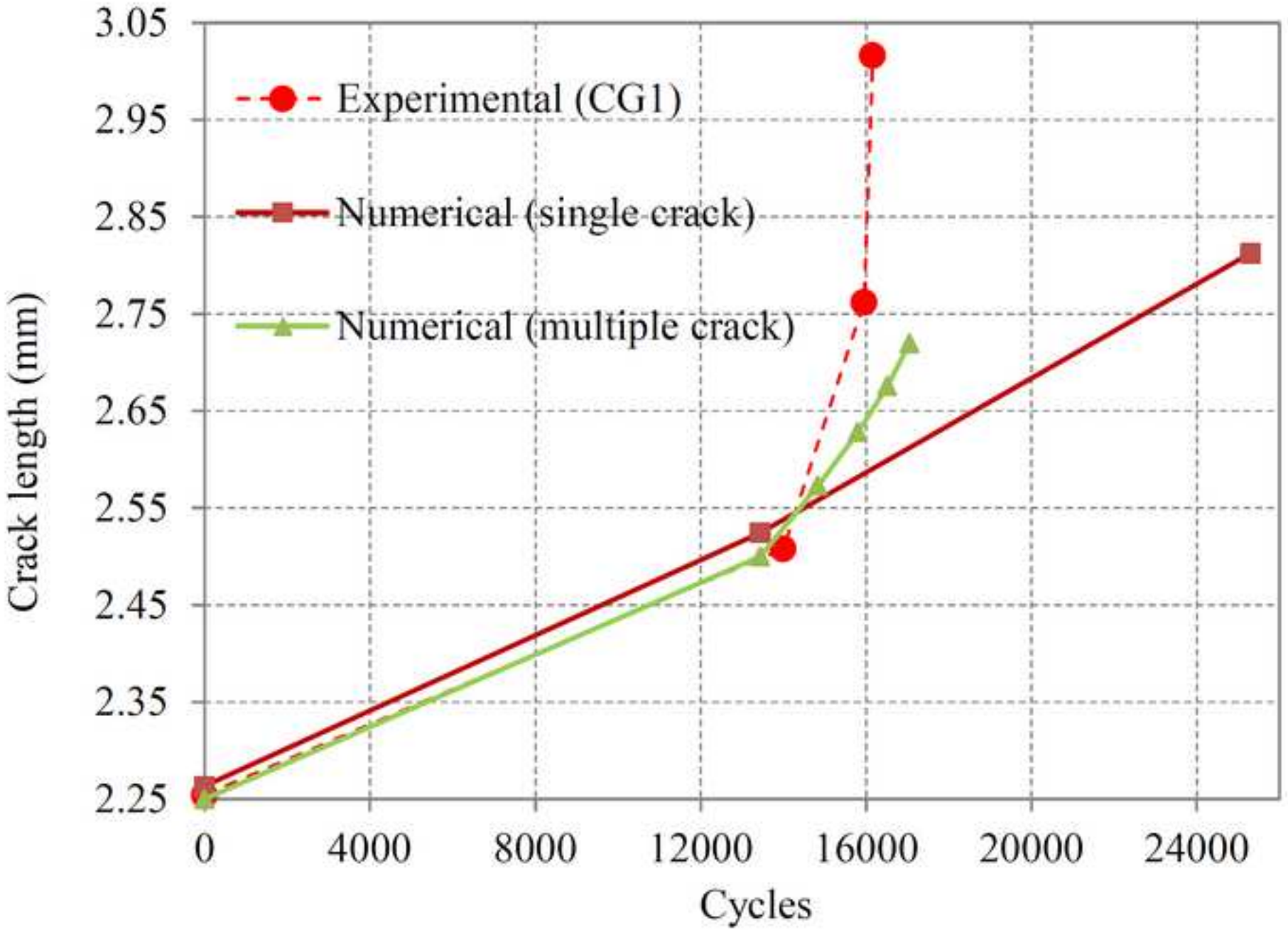

Figure 9

Click here to download high resolution image

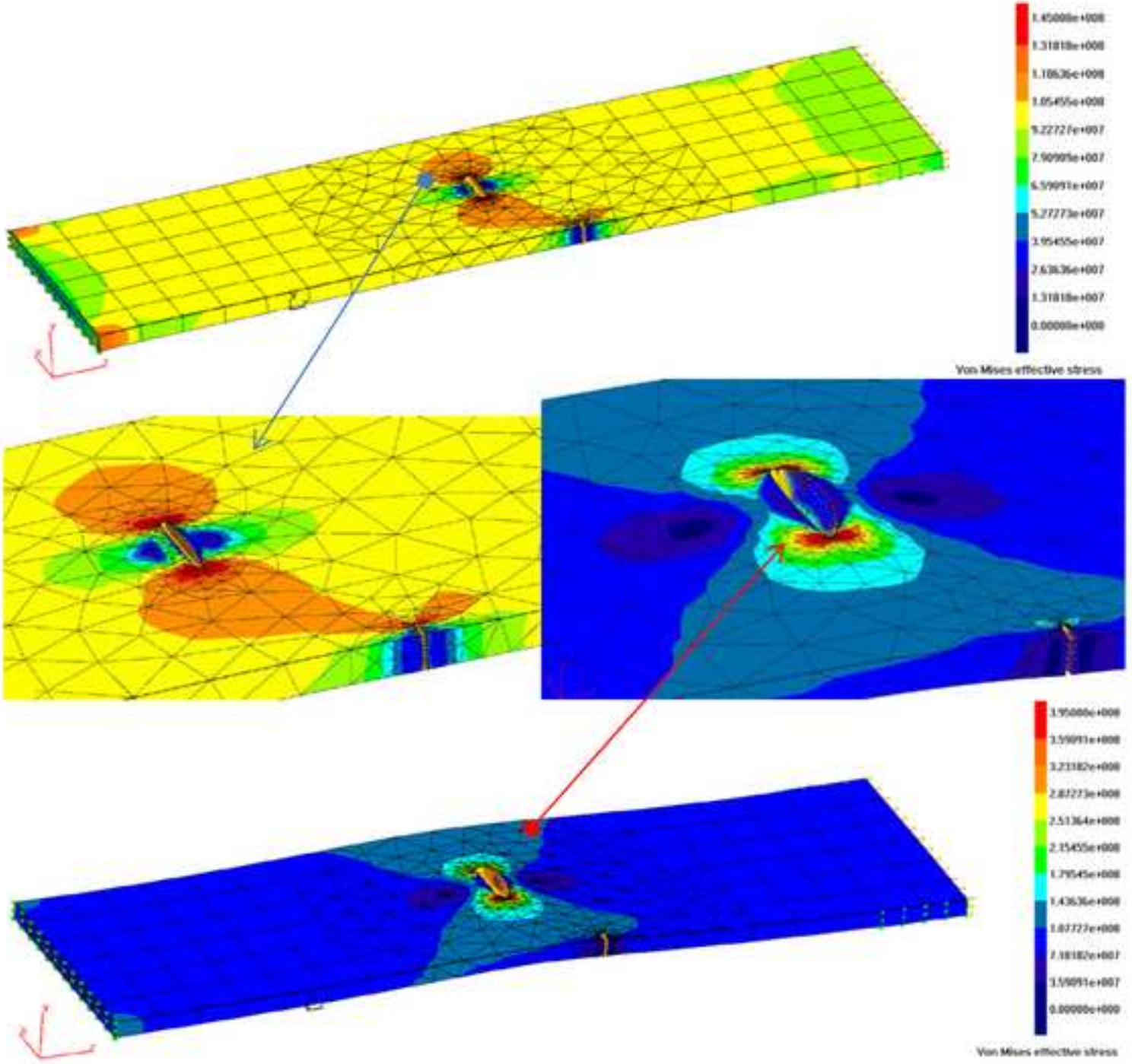

Figure 10

Click here to download high resolution image

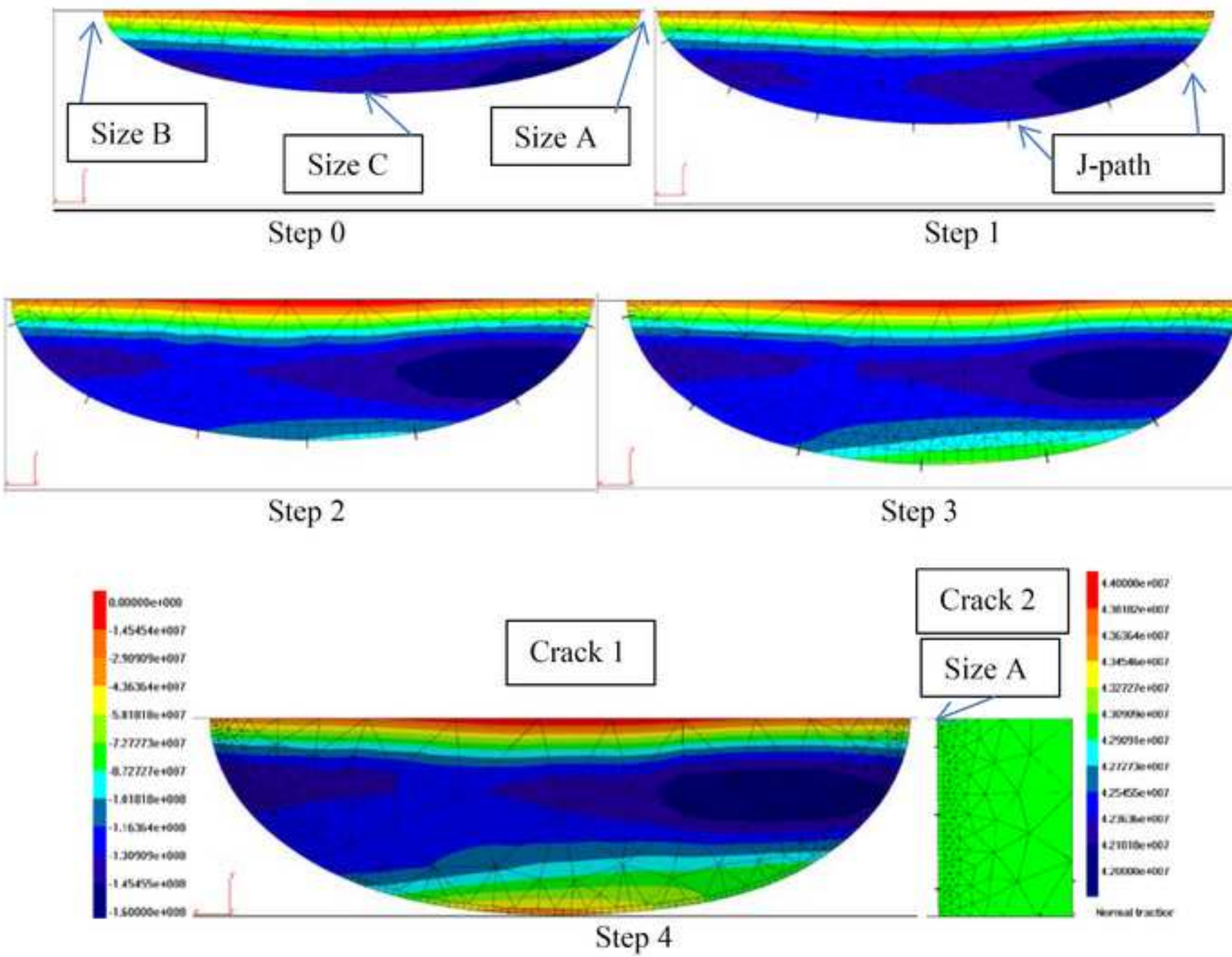

Figure 11
Click here to download high resolution image

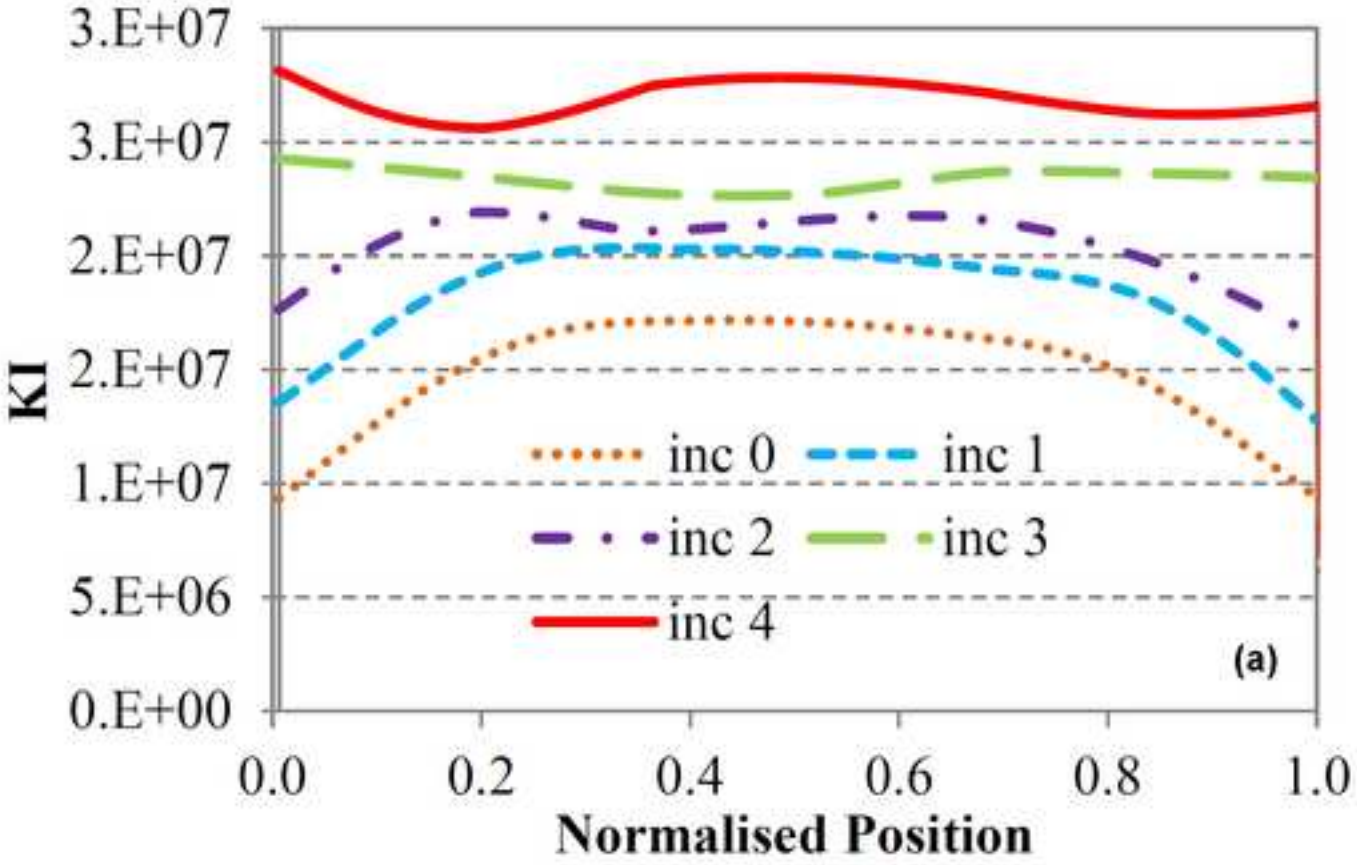

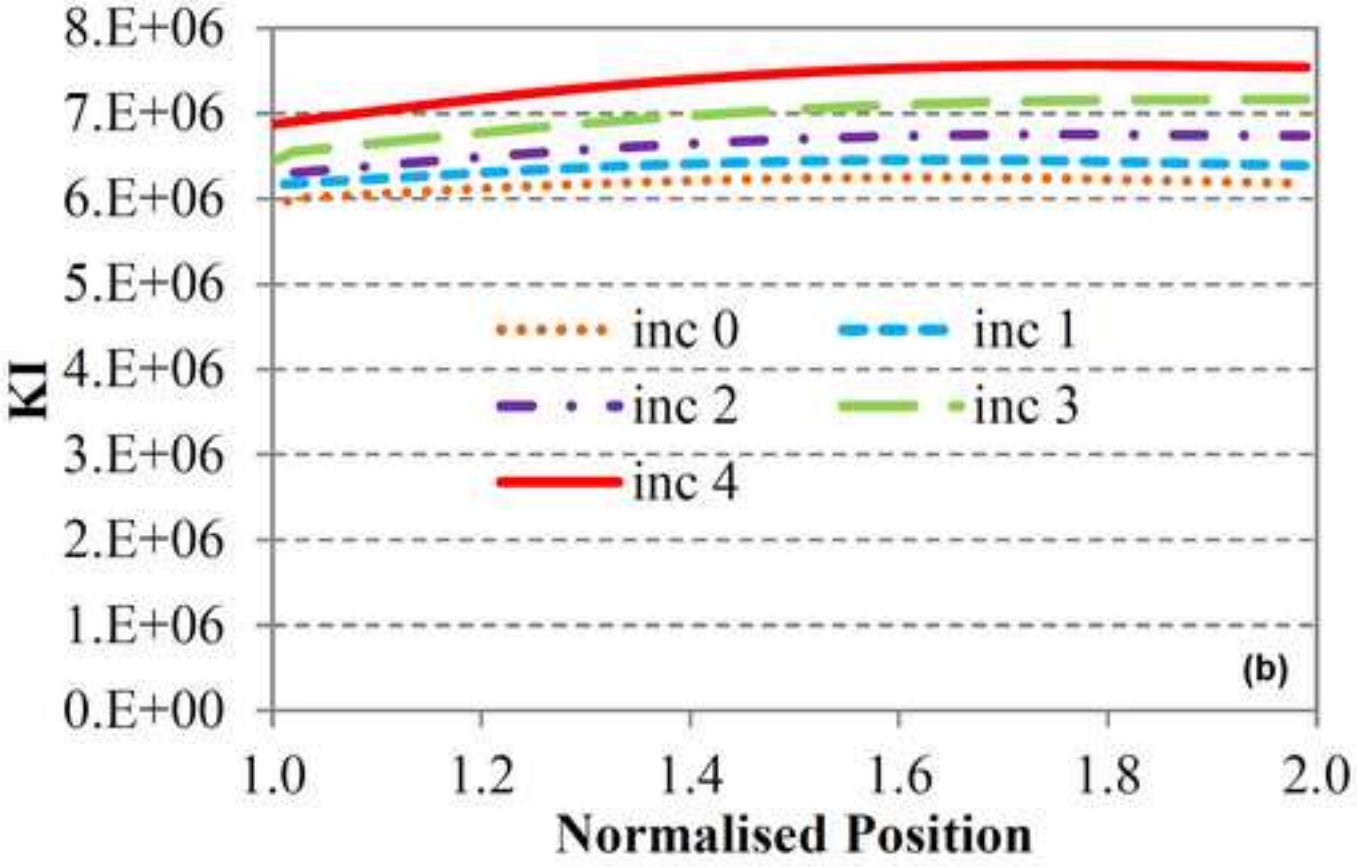

Figure 12

Click here to download high resolution image

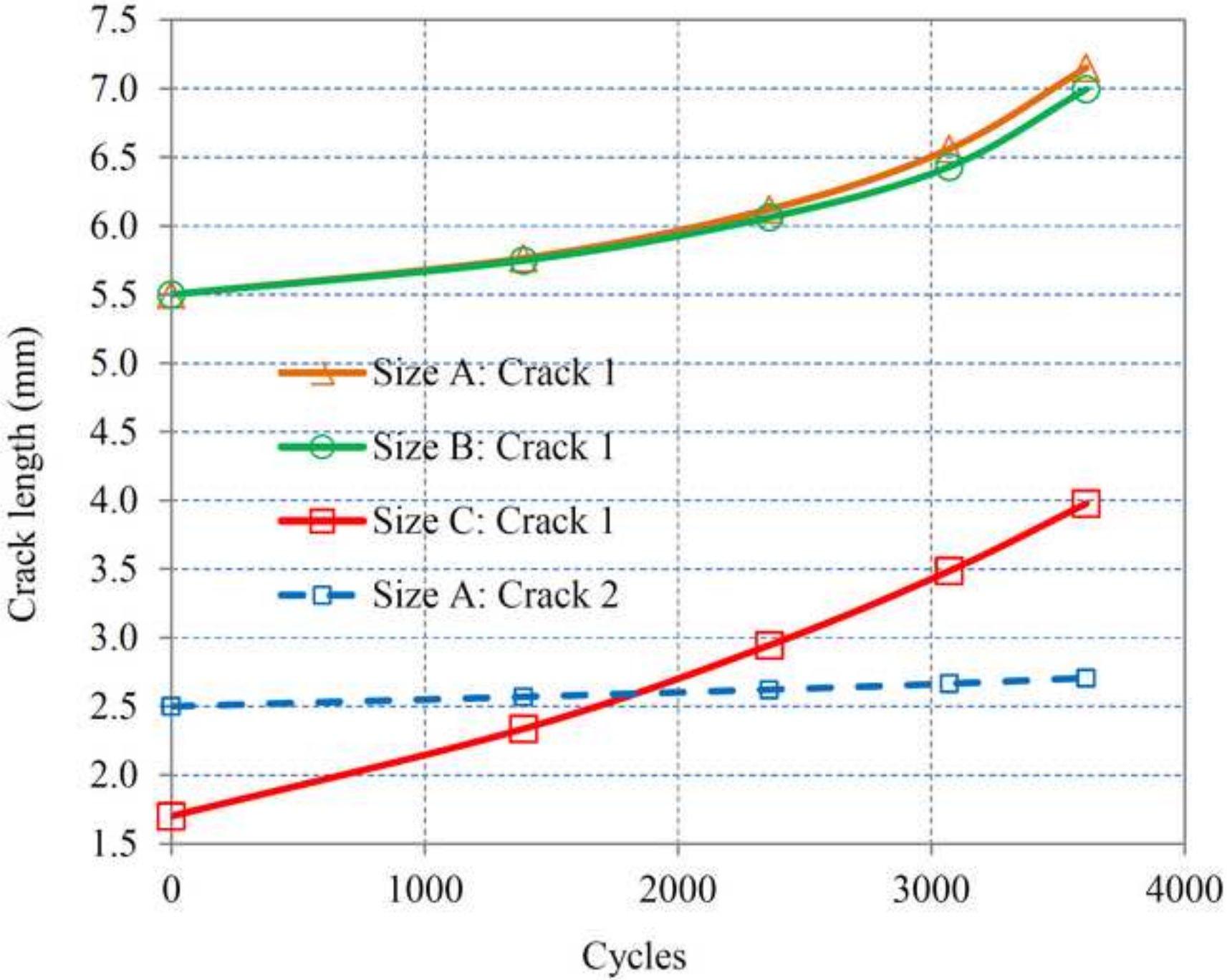

Figure 13
Click here to download high resolution image